

## Research Article

# CO<sub>2</sub> Adsorption: Experimental Investigation and CFD Reactor Model Validation

Ronald W. Breault,<sup>1</sup> Lawrence J. Shadle,<sup>1</sup> James L. Spenik,<sup>2</sup> and E. David Huckaby<sup>1</sup>

<sup>1</sup> National Energy Technology Laboratory, U.S. Department of Energy, Morgantown, WV 26507, USA

<sup>2</sup> REM Engineering Services, Morgantown, WV 26507, USA

Correspondence should be addressed to Ronald W. Breault; [ronald.breault@netl.doe.gov](mailto:ronald.breault@netl.doe.gov)

Received 28 July 2014; Revised 3 October 2014; Accepted 6 October 2014; Published 30 October 2014

Academic Editor: Changbing Yang

Copyright © 2014 Ronald W. Breault et al. This is an open access article distributed under the Creative Commons Attribution License, which permits unrestricted use, distribution, and reproduction in any medium, provided the original work is properly cited.

The National Energy Technology Laboratory is investigating a new process for CO<sub>2</sub> capture from large sources such as utility power generation facilities as an alternative to liquid amine based adsorption processes. Many of these advanced dry processes are based upon sorbents composed of supported polyamines. In this analysis, experiments have been conducted in a laboratory-scale fluidized bed reactor and compared to CFD reactor predictions using kinetics obtained from TGA tests. Batch experiments were conducted by flowing a mixture of CO<sub>2</sub>, H<sub>2</sub>O, and N<sub>2</sub> (simulated flue gas) through a fluidized bed of sorbent material. The exit gas composition time series data is compared to CFD simulations using a 3-dimensional nonisothermal reacting multiphase flow model. The effects of the gas flow rate, distributor design, and particle size are explored through the CFD simulations. It is shown that the time duration for CO<sub>2</sub> adsorption decreased for an increase in the gas flow. Fluid bed hydrodynamics indicated that there were regions in the reactor where the inert FCC particles segregated and defluidized; without adversely affecting the capacity of the sorbent to adsorb CO<sub>2</sub>. The details of the experimental facility and the model as well as the comparative analysis between the data and the simulation results are discussed.

## 1. Introduction

Over the past two to three decades, there has been increasing concern over the importance of carbon dioxide emissions to the environment and the possible effect these emissions have on global climate shifting. Historical atmospheric CO<sub>2</sub> levels have been greater and less than the preindustrialized values shown in Figure 1 [1]. Also shown in Figure 1 are the CO<sub>2</sub> concentration levels over the past 30 years [2]. These values start in 1980 with a concentration of 338 ppm, already outside the normal range over the past 400,000 years, and increase to a value of 392 ppm in 2012, the last year that data exist. Based on these CO<sub>2</sub> numbers there is little doubt that CO<sub>2</sub> is higher now than in the recent past. Extrapolating the trend in the data taken over the past 30 years backwards (Figure 1) this trend intersects with that of the historical data in the time frame of the beginning of the industrial age. This implies with strong confidence that the increased values of CO<sub>2</sub> are likely caused from human activity. The recent divergence between

the temperature data and the CO<sub>2</sub> concentration data refutes assertions that global warming can be attributed to increased CO<sub>2</sub> concentration as does the trend in the temperature variation between 1940 and the late 1970s [3]. Even so, the buildup of CO<sub>2</sub> in the atmosphere, whether leading to climate change or not, is attributed to human activity (combustion of fossil fuels associated with industrial and power production) and as such it is prudent of us to investigate mitigation approaches such as the CO<sub>2</sub> capture technology discussed below.

The U.S. Department of Energy has set goals for carbon capture systems at 90% carbon dioxide (CO<sub>2</sub>) capture with less than a 35% increase in cost of electricity [4]. In this approach, the fossil energy system is designed or retrofitted such that a relative pure stream of CO<sub>2</sub> can be separated from the exhaust. The exhaust can then be utilized or sequestered. There are four main categories of these technologies: precombustion, postcombustion, oxy-fuel combustion, and chemical looping [5].

TABLE 1: Summary of literature capture concepts.

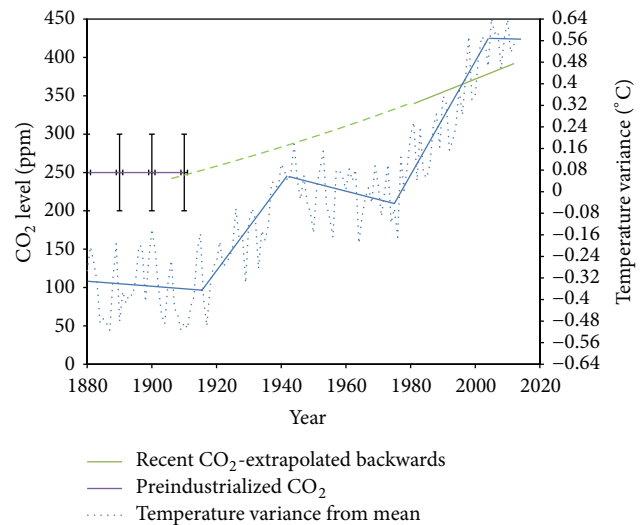
Author	Sorbent	Reactor concept	Experimental reactor concept
Hasan et al. [12]	13X Zeolite	PSA and VSA	N/A
Chaffee et al. [13]	13X Zeolite	VSA	N/A
Schell et al. [14]	Activated Carbon	PSA	Fixed bed
Wang et al. [15]	13X Zeolite and activated carbon	VPSA	Fixed bed
Pirngruber and Leinekugel-Le-Cocq [16]	Supported polyamine	PSA	N/A
Siriwardane et al. [17]	NaOH/CaO	TSA	TGA and fixed bed
Fauth et al. [18]	Supported mixed amines	TSA	Fixed bed
Gray et al. [19]	Supported tertiary amine	TSA	TGA and fixed bed
Gray et al. [20]	Supported amine	TSA	TGA
Lee et al. [21]	Supported amine	TSA	TGA
Sjostrom et al. [22]	Supported amine	TSA	CFB
Sjostrom and Krutka [23]	Supported amine	TSA	Fixed bed
Monazam et al. [24]	Supported amine	TSA	Fluidized bed

Postcombustion capture technologies include liquid solvent and solid sorbent systems [6]. Since there is a large existing fleet of coal fired power plants, these technologies are particularly beneficial as they are well suited for retrofit installations. Furthermore, since they are added to the back-end of the power plant they clean the exhaust of  $\text{CO}_2$  without necessarily change the normal plant operation. The solid sorbent systems can be further divided into low and high temperature systems [7–11].

An overview of the literature [12–24] and the various sorbent reactor configurations is presented in Table 1. Samanta et al. [25] and Choi et al. [26] provide comprehensive reviews of sorbent processes employing temperature swing, pressure swing, or vacuum swing to regenerate the adsorbate, referred to as PSA, TSA, and VSA concepts, respectively. The TSA concepts have gained favor recently because the polyamine impregnated sorbents which have strong temperature dependence in the temperature range of interest can be made with high  $\text{CO}_2$  capacity [17–24].

The absolute pressure of flue gas exiting a conventional pulverized coal-fired combustor is relatively low as well as the  $\text{CO}_2$  partial pressure. Given this fact, the temperature swing option for adsorption/desorption appears to be the more viable option when amine-based solid sorbents are used [27]. Also, the use of a solid substrate impregnated with and amine compound is a superior alternative to that of a water based solution of amine due to the lower specific heat of the solid substrate compared to an aqueous carrier. By moving the sorbent between regions of adsorption and desorption a more efficient system can be achieved.

Numerous reactor types have been employed and proposed for regenerable dry  $\text{CO}_2$  capture systems. Even though investigated extensively at small scale, fixed bed reactors have considerable design issues when employed at the utility scale. The most significant of these being reactor heating and cooling as well gas ducting, piping, and valving. In contrast, fluidized bed systems are known for good heat transfer allowing for smaller reactors and have no issues associated with gas ducting, piping, or valving.

FIGURE 1: Global temperature and  $\text{CO}_2$  levels (data taken from [1–3]).

The system investigated here is a circulating fluidized bed. This system has the advantage over a fixed bed system in that the sorbent can be moved from the adsorption region where exothermic reactions occur and heat must be removed to a regeneration region where the reaction is endothermic and heat must be added. These regions can be maintained at a fixed temperature in a circulating bed operation whereas in a fixed bed concept considerable energy must be added and removed from containment vessels. In a circulating bed, the only energy transfer required is for heating or cooling of the substrate, chemical reaction, and environmental losses.

Fluidized bed reactors have been used to evaluate adsorption and regeneration using these promising polyamine sorbents [22, 24, 28]. Pilot studies using coupled fluidized beds reported a number of operational difficulties that were thought to be associated with desorption kinetics [22]. Unfortunately, fluid bed desorption studies have been limited

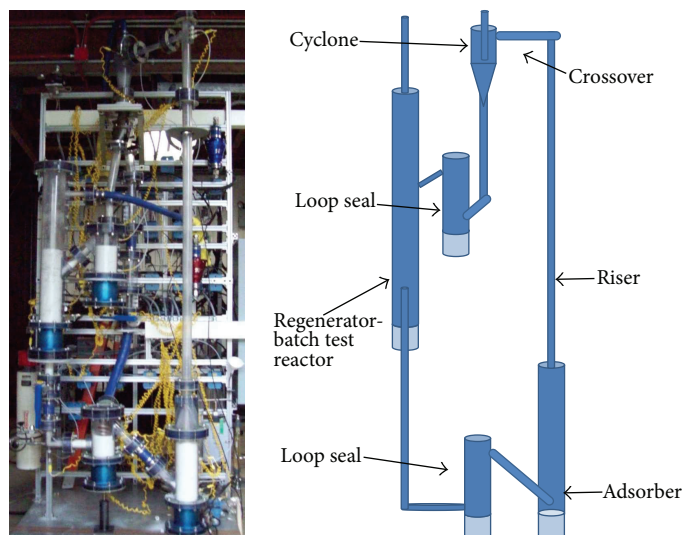


FIGURE 2

to a very few tests over a narrow range of temperatures,  $\text{CO}_2$  compositions, and levels of conversion [28]. More information is available on the adsorption process. Kinetic analysis for fluid bed adsorption in these sorbents was consistent with the TGA data [24, 29]; however, the proposed nucleation and growth rate expressions are too numerically unstable to incorporate into computationally intensive CFD models.

As a preliminary step in the investigation of a computational method to simulate the experimental system only the adsorption phase was considered in a batch phase. When a satisfactory result is obtained the simulation can be extended to include regeneration and full loop operation.

This work focuses on computational fluid dynamics (CFD) simulations and experiments of adsorption and regeneration using amine-based solid sorbent in a fluidized bed. This is part of ongoing investigations at NETL on  $\text{CO}_2$  capture using solid-sorbents experiments and simulation [30–33]. In this study, the simpler kinetic expression was employed to describe the  $\text{CO}_2$  adsorption process. This study was undertaken to determine whether the sorption process could be adequately simulated using this simplified expression and how the reactor internals influenced mixing and the resulting  $\text{CO}_2$  breakthrough profiles.

## 2. Solid Sorbent Carbon Capture System

A photograph of the experimental facility is shown along with a line drawing in Figure 2. The facility consists of an adsorber and riser on the right and the regenerator on the left. Sorbent particles under normal operation travel up the riser from the adsorber across the crossover and are separated from the  $\text{CO}_2$  lean flue gas in the cyclone. The  $\text{CO}_2$  loaded sorbent exits the cyclone bottom passing through the diverter valve and loop seal to the regenerator. The regenerated sorbent exits the bottom of the regenerator, passing through another loop seal and is returned to the adsorber. The diverter valve is used

for short periods to measure the solids circulation rate. The specific batch experiments were conducted in the regenerator, the details of which are presented below.

The reactor (regenerator vessel) is comprised of a section of high density polyethylene 16.5 cm OD, 13.7 cm ID, 1.04 m long. A plenum was attached below the reactor where gases are introduced. The plenum as shown in Figure 3 is separated from the reactor by a sintered metal distributor plate which allows gas flow into the reactor. A 5.1 cm ID tube connects the regenerator to the bottom loop seal. This allows the solids to be withdrawn from the center of gas distributor when the unit is run in the full loop mode. For semicontinuous or batch tests this tube was sealed off by closing the valve below the plenum. Both  $\text{N}_2$  and  $\text{CO}_2$  flows were controlled using Alicat 0–50 slpm mass flow controllers. Humidification was accomplished using a Bronkhorst controlled evaporator mixer. Temperatures were measured using thermocouples at positions 1.0, 15.0, and 35 cm above the distributor plate.  $\text{CO}_2$  concentrations were determined using a PP systems WMA-4  $\text{CO}_2$  analyzer (0–10,000 ppm range). The low range of the analyzer required the introduction of dilution gas (air) to the stream which was also controlled using an Alicat mass flow controller.

Heating/cooling is accomplished by flowing oil through copper coils immersed in the bed. When heating, the oil is passed through Cromolox heater where the oil temperature is controlled to yield the desired bed temperature. During cooling phases, the oil is passed through coils immersed in a cooled water bath then to the bed coils. There are two sets of coils, the outer coil consists of 1.27 cm OD copper tubing, 4.4 meters in length. The outer coil is a 1.57 cm diameter helix with vertical separation of 2.54 cm between the coils center to center. The inner coils are comprised of 0.95 cm OD copper tubing, 3.0 meters in length. The inner coil is a 5.08 cm diameter helix with vertical separation of 1.9 cm between the coils center to center. The sorbent mixture

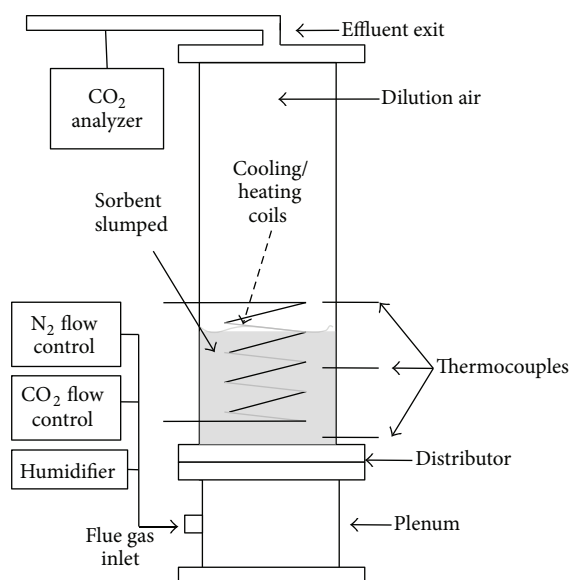


FIGURE 3: Details of adsorption reactor used in tests.

TABLE 2: Experimental conditions.

Cycle phase	Plenum N <sub>2</sub> slpm	Plenum H <sub>2</sub> O-vapor slpm	Plenum CO <sub>2</sub> slpm	Total plenum flow slpm
Pretreatment	30	0.6	0	30.6
Transition to adsorption	30	0.6	0	30.6
Adsorption	See below	0.6	See below	See below
Transition to regeneration	30	0.6	0	30.6
Regeneration	30	0.6	0	30.6
Adsorption-60	49.8	1.2	9.0	60
Adsorption-30	24.9	0.6	4.5	30
Adsorption-15	12.5	0.3	2.25	15

is pretreated to remove any previously adsorbed CO<sub>2</sub> by exposing the bed to N<sub>2</sub> flow of 30 slpm and heating the bed to 110°C. When the CO<sub>2</sub> concentration dropped to negligible levels the bed was cooled to 70°C under humidified N<sub>2</sub> flow. After the desired bed temperature was achieved the desired mixture of CO<sub>2</sub>/N<sub>2</sub> flow was introduced. This flow was continued until the CO<sub>2</sub> flow at the outlet matched the inlet flow indicating the sorbent had reached its capacity. The sorbent was then heated to 110°C under humidified N<sub>2</sub> flow and maintained at that temperature until the outlet CO<sub>2</sub> concentration was negligible. The bed was then cooled to the adsorption temperature and another adsorption condition was run. A summary of the experimental test conditions is presented in Tables 2 and 3. The flow rate information is presented in Table 1 while the adsorption/regeneration cycle information is presented in Table 2.

### 3. Particle Properties and Sorbent Chemistry/Kinetics

**3.1. Sample Preparation and Characterization.** Sorbent AX was nominally 40% polyethylenimine (PEI) [BASF] on a

TABLE 3: Operational cycles.

Cycle phase	Bed temperature °C	Dilution air slpm
Pretreatment	110	90
Transition to adsorption	110–70	90
Adsorption	70	90
Transition to regeneration	70–110	90
Regeneration	110	90

silica substrate. A photomicrograph of this material is shown in Figure 4 using a Leica M205 FA microscope under white reflected light. FCC particles were smooth round particles of various shades of gray as a result of the coking in the petroleum refining process, while the sorbent particles were asymmetric larger white particles. The active ingredient in the sorbent is a polymer of 1,2-ethanediamine and aziridine which was dissolved into methanol, added to the silica substrate, and then the solvent was evaporated off. The substrate was a high surface area mesoporous silica (PQ Inc. 2129) with N<sub>2</sub> BET surface area of 312 m<sup>2</sup>/g [21].

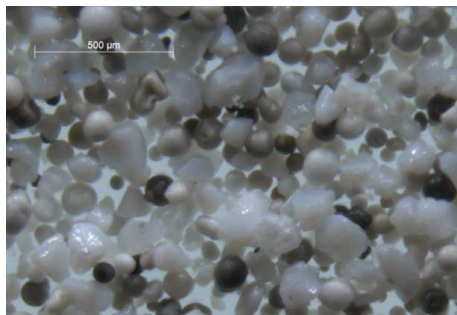


FIGURE 4: Photomicrograph of 80 : 20 wt% mixture of used FCC and Sorbent AX (courtesy of Yael Tucker, NETL).

TABLE 4: Particle properties.

	AX sorbent	FCC
Individual:		
Intrinsic density (g/cc)	0.94	1.41
Sauter mean ( $\mu\text{m}$ )	115	90
Sphericity	0.90	0.93
$U_{mf}$ (cm/s)	0.52	0.36
Mass (kg)	0.34	1.36
Composition:		
PEI (%)	40	—
Silica (%)	60	—
Capacity (moles $\text{CO}_2$ /kg sorbent)	$2.7 \pm 0.1$	—
Mixture:		
Fraction of total mass	0.20	0.80
Fraction of total volume	0.27	0.73

Initial experiments with 100% sorbent particles and relatively deep beds produced breakthrough times in excess of 1 hour, a time scale nearly impossible to simulate for CFD, since the simulations typically provide about 30 seconds of data per day. In this case, the simulations would need to run for more than six months to simulate a single case. Engineering analysis of the breakthrough data revealed that experiments could be designed to provide breakthrough times of less than 600 seconds by correctly choosing the sorbent bed material. The sorbent bed in these experiments and simulations consists of 80% FCC and 20% sorbent. The material properties are presented in Table 4.

The particle size was measured using QICPIC particle imaging analyzer (Sympatec GmbH, Model-QP0104). The particle size distribution for the mixture was Gaussian as displayed in Figure 5. The Sauter mean size of the FCC, sorbent AX and 80:20 mixture are presented in Table 4 along with other relevant hydrodynamic and  $\text{CO}_2$  adsorption properties. The particle size of the FCC was slightly greater than that of the sorbent. This compensated for the FCC's higher density to produce similar hydrodynamic properties.

The minimum fluidization velocity was measured using a 5 cm diameter fluidized bed with porous sintered metal

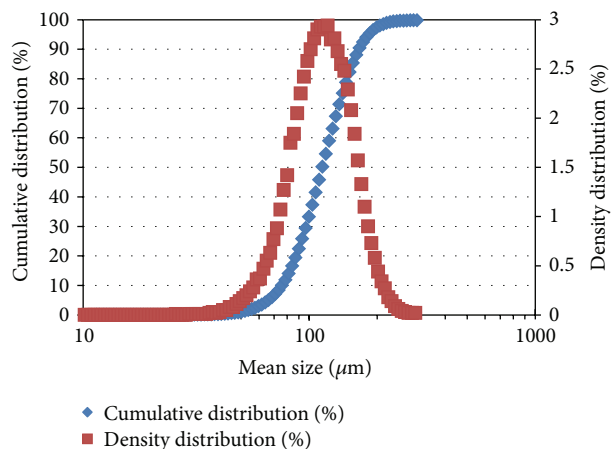


FIGURE 5: Particle size distribution of 20 : 80 Sorbent : FCC mixture (by wt.).

gas distributor. This velocity represented the intersection of two nominally linear regions (packed bed and fluid bed) in the plot of pressure drop across the granular bed against gas velocity (Figure 6). The pressure drop was normalized by the weight of the fluid bed. These materials were classified as Geldart Group A materials based upon their behavior and the relative densities and particle sizes. The sorbent  $\text{CO}_2$  uptake behavior was measured in fluid bed [26]. Sorbent capacities for  $\text{CO}_2$  uptake were between 86 and 122 mg/g sorbent depending on temperature and, to a lesser extent,  $\text{CO}_2$  concentration. The 20 : 80 mixture of sorbent and FCC resulted in a molar capacity of 0.54 moles  $\text{CO}_2$ /kg sorbent which along with short sorbent beds facilitated timely CFD simulations.

**3.2. Chemistry/Kinetics.** Abbasi, Choi, Fauth, Gray, and Sjostrom [18–20, 22, 23, 26, 34] have all considered mesoporous materials for sorbents in carbon capture systems. The work presented in this paper is based on a silica-supported amine sorbent material developed at NETL. This material is very similar to the materials described by both Gray et al. [19, 20] and Fauth et al. [18]. The  $\text{CO}_2$  adsorption process is modeled utilizing mechanism that is similar to the one proposed by Lee et al. [21] for a similar sorbent for a dry reaction. The  $\text{CO}_2$  absorption process is expressed as the reaction of gaseous  $\text{CO}_2$  with two amine ( $\text{R}_2\text{NH}$ ) sites to produce a carbamate ion ( $\text{R}_2\text{NCO}_2^-$ ) and protonated amine ion ( $\text{R}_2\text{NH}_2^+$ ):



This work utilizes the “volume-average” reaction model in Barracuda for the simulations presented in this paper. The



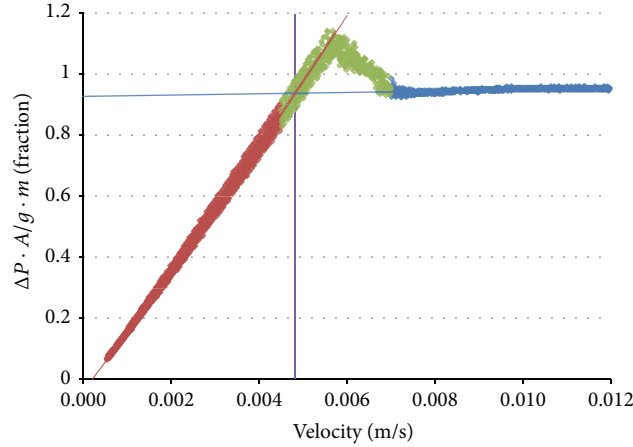


FIGURE 6: Minimum fluidization curve for sorbent AX.

adsorption (forward) and desorption (reverse) rates ( $\text{kmol-CO}_2/\text{m}^3\text{-s}$ ) take the form

$$R_{\text{abs}} = AT^b p^c \exp\left(-\frac{E}{T} + E_0\right) \frac{1}{\alpha_s} \left(\frac{m_A}{V_{\text{cell}}}\right)^2 [\text{CO}_2], \quad (2)$$

$$R_{\text{des}} = AT^b p^c \exp\left(-\frac{E}{T} + E_0\right) \frac{1}{\alpha_s} \left(\frac{m_B}{V_{\text{cell}}}\right)^2,$$

where  $m_A$  is the total mass amine in a given cell and  $m_B$  is the mass of the carbamate ion. It was assumed in the derivation of the above expressions that the molar concentration of the protonated amine ion is equal to the concentration of the carbamate ion. The values of the coefficients used in the simulations are provided in the rate expressions are provided Breault and Huckaby [32]. The values of  $E$  and  $E_0$  were tuned so that the predicted  $\text{CO}_2$  in the exhaust matched the experimental measurement at the baseline condition as reported by Sjoström et al. [22] while holding the  $A$  values equal to those presented by Lee et al. [21] after conversion of the units. Lee et al. [21] describe the chemical kinetics of  $\text{CO}_2$  adsorption on PEI impregnated mesoporous silica sorbents in more detail.

The silica substrate is considered an open sorbent with micropores and a network of tubular shaped mesopores which consist of silica-PEI composite structures depicted in the right hand close up of the PEI loaded mesopores. Monazam et al. [29] found that a mesoporous PEI based sorbent exhibits 2-dimensional nucleation growth diffusion controlled rates within this composite structure. The adsorption rate is controlled by the transport of  $\text{CO}_2$  into the deeper PEI layers in the mesopores. In addition, it was demonstrated that the bulk and macroporous diffusion is fast compared to the sorption rate within the mesopores. However, when analyzing fluidized beds  $\text{CO}_2$  breakthrough results Monazam et al. [24] found that the effective rate could be adequately modeled using first order Arrhenius kinetics with a negative temperature dependence providing confidence that the above kinetic models can reasonably be used in CFD simulations to predict  $\text{CO}_2$  capture.

#### 4. Numerical Model

Barracuda [35] is a CFD code developed by CPFD Software which was used to perform the simulations in this study. Barracuda is based upon the multiphase particle-in-cell (MP-PIC) model developed by Andrews and O'Rourke [36] and Snider [37]. Barracuda is a discrete particle simulation tool (or Eulerian-Lagrangian) tool [33], where the particles are treated in a Lagrangian manner while the fluid conservation equations are solved using Eulerian equations. The effects of particle-particle collisions in MP-PIC are approximated on the gas continuum by utilizing a pressure proportional to the particle concentration. Furthermore, the parcel or cloud concept is introduced to allow the simulation of systems with large numbers of particles. Parcels or clouds are groups of particles which are assumed to have the same position, velocity, and properties. Therefore, the dynamics of any particle in the group can be derived from the equations of one particle in the parcel or cloud. Parcels or clouds are also referred to as computational particles and computational parcels.

O'Rourke and Snider [38] made some additional improvements to the momentum balance of the particle phase by adding a particle-particle "drag" term. This term is in addition to the typical "gas-solid" drag and the granular pressure terms. The form of the mass, species mass, momentum, and energy equations for the fluid-phase has been given by Snider et al. [39] and Snider and Banerjee [40]. These equations were derived from Anderson and Jackson [41] and Jackson [42] and are discussed below.

CPFD's Barracuda code solves the fluid and particle equations in three dimensions using the averaged Navier-Stokes equations. Strong coupling of the particle phase with the fluid phase is obtained in the code utilizing the concepts developed by Snider et al. [39] and Snider and Banerjee [40]. The particle momentum equation uses the multiphase particle-in-cell (MP-PIC) concept as initially developed by Andrews and O'Rourke [36] including modifications to it by Snider [37]. That work was further refined by O'Rourke and Snider [38] to include a "relaxation-to-the-mean" term

to represent damping of particle velocity fluctuations due to particle collisions. Mass, momentum, and energy of the two-phase mixture are conserved by exchange terms in the gas phase mass, momentum, and energy equations, respectively. Therefore, in summary, the mass and momentum equations for the fluid-phase are averaged forms of the detailed fluid-phase mass and momentum equations [39] and [40] and are presented in (3)–(18) as follows.

*Equations Used in Barracuda.* Consider

$$\frac{\partial(\alpha_f \rho_f)}{\partial t} + \nabla \cdot (\alpha_f \rho_f \mathbf{u}_f) = \delta \dot{m}_p, \quad (3)$$

$$\begin{aligned} \frac{\partial(\alpha_f \rho_f \mathbf{u}_f)}{\partial t} + \nabla \cdot (\alpha_f \rho_f \mathbf{u}_f \mathbf{u}_f) \\ = -\nabla P + F + \alpha_f \rho_f \mathbf{g} + \nabla \cdot (\alpha_f \boldsymbol{\tau}_f), \end{aligned} \quad (4)$$

$$\tau_{f,ij} = \mu \left( \frac{\partial u_i}{\partial x_j} + \frac{\partial u_j}{\partial x_i} \right) - \frac{2}{3} \mu \delta_{ij} \frac{\partial u_i}{\partial x_i}, \quad (5)$$

$$\mu_t = C \rho_f \Delta^2 \sqrt{\left( \frac{\partial u_i}{\partial x_j} + \frac{\partial u_j}{\partial x_i} \right)^2}, \quad (6)$$

$$\begin{aligned} \frac{\partial(\alpha_f \rho_f Y_{f,i})}{\partial t} + \nabla \cdot (\alpha_f \rho_f Y_{f,i} \mathbf{u}_f) \\ = \nabla \cdot (\rho_f D \alpha_f \nabla Y_{f,i}) + \delta \dot{m}_{i,\text{chem}}, \end{aligned} \quad (7)$$

$$\frac{\mu}{\rho_f D} = Sc, \quad (8)$$

$$P_i = \frac{\rho_f Y_{f,i} R T_f}{M w_i}, \quad (9)$$

$$P = \sum_{i=1}^{N_s} P_i, \quad (10)$$

$$f = f(x_p, u_p, m_p, T_p, t), \quad (11)$$

$$N_p = f(x_p, u_p, m_p, T_p, t) du_p dm_p dT_p, \quad (12)$$

$$\delta \dot{m}_p = - \iiint f \frac{dm_p}{dt} dm_p du_p dT_p, \quad (13)$$

$$\frac{du_p}{dt} = D_p (u_f - u_p) - \frac{1}{\rho_p} \nabla P - \frac{1}{\alpha_p \rho_p} \nabla \tau_p + \mathbf{g} + \frac{\bar{u}_p - u_p}{\tau_D}, \quad (14)$$

$$\alpha_p = \iiint f \frac{dm_p}{\rho_p} dm_p du_p dT_p, \quad (15)$$

$$\alpha_f = 1 - \alpha_p, \quad (16)$$

$$F = - \iiint f \left\{ m_p \left[ D_p (u_f - u_p) - \frac{\nabla P}{\rho_p} \right] + u_p \frac{dm_p}{dt} \right\} \times dm_p du_p dT_p, \quad (17)$$

$$\frac{dx_p}{dt} = u_p. \quad (18)$$

In these equations,  $\alpha_f$  is the fluid volume fraction,  $\rho_f$  is fluid density,  $u_f$  is the fluid velocity vector,  $\delta \dot{m}_p$  is the gas mass production rate per volume from gas-particle chemistry,  $P$  is the mean flow gas thermodynamic pressure,  $F$  is the inter-phase momentum transfer rate per unit volume,  $g$  is the gravitational acceleration, and  $\tau_f$  is the fluid stress tensor.

The equation for the fluid stress tensor,  $\tau_f$ , is presented in (3)–(18) where  $i$  and  $j$  are direction and  $\mu$  is shear viscosity, which is the sum of the laminar shear viscosity and a turbulence viscosity. Large eddies are calculated with the unresolved subgrid turbulence being modeled with an eddy-viscosity also presented in (3)–(18) and identified as (6). In this equation,  $C$  is the Smagorinsky [43] coefficient (0.01) and  $\Delta$  is the subgrid length scale which is the cube root of the sum of the product of orthogonal distances across a calculation cell.

The transport equations are solved for each gas species with the total fluid phase properties calculated from the mass fractions  $Y_{f,i}$  of the gas species  $i$ . Mass is transferred between gas species through the breaking and forming of chemical bonds with a chemical source terms  $\delta \dot{m}_{i,\text{chem}}$  in the individual gas species transport equations (see (3)–(18)) where  $D$  is the turbulent mass diffusivity and is related to the viscosity by the definition of the Schmidt number.

The mass balance and momentum balances for the gas mixture are presented in (3) and (4), respectively. The gas mixture properties are based on the mass fractions of the gas species, solved for using (7). Moreover, the flow is compressible, and the gas phase pressure, density, and mass fractions are related through the ideal gas equation of state. Using the ideal gas equation, the partial pressure of gas species  $i$  is presented as (9) where  $R$  is the universal gas constant,  $T_f$  is the gas mixture temperature, and  $M w_i$  is the molecular weight of gas species  $i$  and the total mean flow gas thermodynamic pressure is obtained by (10).

In Barracuda, the dynamics of the particle phase are predicted by solving a transport equation for the particle distribution function (PDF),  $f$ . This function is based upon the work of [36] in their development of the MP-PIC methodology. Barracuda assumes that the particle distribution function is a function of particle spatial location ( $x_p$ ), particle velocity ( $u_p$ ), particle mass ( $m_p$ ), and particle temperature ( $T_p$ ), and time ( $t$ ) is represented by (11). The average number of particles per unit volume,  $N_p$ , is obtained from the velocities in the interval ( $u_p, u_p + du_p$ ), masses in the interval ( $m_p, m_p + dm_p$ ), and temperature in the interval ( $T_p, T_p + dT_p$ ) as shown in (12).

In CPFD's Barracuda, the fluid mass source term from (3) is presented as (13) where the time-rate-of-change of

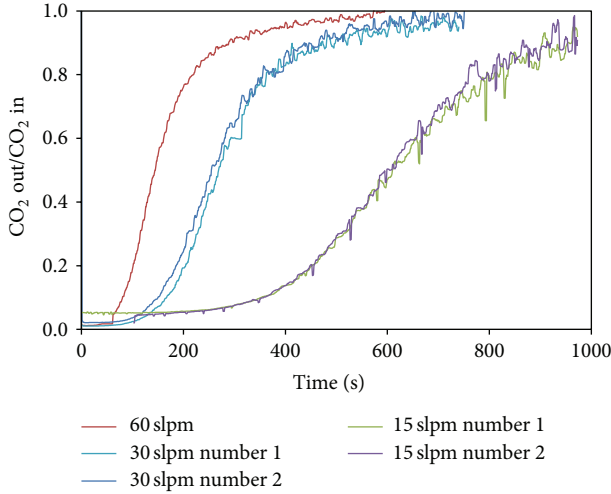


FIGURE 7: Experimental breakthrough data.

particle mass  $dm_p/dt$  is the rate of change of the particle mass producing gasses through chemistry.

Furthermore, the acceleration on a particle is obtained from (14) where  $\alpha_p$  is the solids volume fraction;  $\rho_p$  is the solid material mass density;  $D_p$  is the drag function which depends on the particle size, velocity, position, and time;  $\tau_p$  is the solids contact stress, which depends on spatial location;  $u_p$  is the local mass-averaged particle velocity; and  $\tau_D$  is a particle collision damping time from [39].

The solids volume fraction is related to the particle distribution function,  $f$ , as shown in (15) where the fluid volume fraction is given by (16).

The interphase momentum transfer rate per unit volume,  $F$ , in (4) is found from (17) and, finally, (18) gives the solid displacement. Collectively, these equations and relationships provide the backbone to CPFD's Barracuda code that was used in this work.

## 5. Simulation Results and Analysis

**5.1. Experimental Results.** Five experiments were conducted with the sorbent-FCC mixture. The results from these tests are shown in Figure 7, where the instantaneous outlet concentration normalized by the inlet concentration is plotted against the elapsed time. The breakthrough curves are "classic" S-shaped sigmoidal curves. As expected, the breakthrough time increased with decreasing experimental flow rate. The tests at 30 slpm and 15 slpm were duplicated. There was little difference between the two test results. Using this later to define the test reproducibility, the average absolute percent error (AA%E) is 3.41 and the correlation coefficient between these two tests gives an  $R^2$  value of 0.936.

The measured pressure drop across the fluid beds was  $0.53 \pm 0.009$  kPa and did not vary significantly as the flow varied over the tests described in Table 2. This reflects the fact that all of these experiments were conducted at conditions

TABLE 5: Summary of AA%E and  $R^2$  values.

	AA%E	$R^2$
Experimental repeats	3.41	0.99
15 slpm	8.88	0.941
30 slpm	5.4	0.973
60 slpm	6.32	0.94

well over minimum fluidization. The pressure drop represented less than 60% of the weight of the FCC-sorbent loaded into the bed. This result indicated that either channeling or defluidization occurred which caused a significant portion of the mixture to be supported by the internals, that is, the heat exchange coils, or defluidized in the central region of the bed above the stagnant solids underflow piping. The  $\text{CO}_2$  sorption capacity of the sorbent was not adversely affected by the channeling or defluidization suggesting that the FCC was the preferentially segregated. The sorbent capacities were found to be  $2.61 + 0.22/-0.31$  moles/kg of sorbent by integrating the  $\text{CO}_2$  adsorbed over the duration of each test. The sorbent capacity did not vary substantially with flow.

**5.2. Baseline Studies.** The simulation results are shown in Figures 8(a), 8(b), and 8(c) along with the respective experimental data for the three test conditions. In Figure 8(a),  $\text{CO}_2$  breakthrough was complete by about 900 seconds for the 15 slpm tests. The AA%E and the correlation coefficient  $R^2$  between simulation and the average experimental value is 8.88 and 0.941, respectively. Recall from above that the error between experimental repeats had an AA%E of 3.41 and an  $R^2$  of 0.99. The error between the simulation and the experiment is smaller than the error between the experimental repeats—that is the best that can be expected. These error values are summarized in Table 5.

The experimental data for the cases using a flow rate of 30 slpm is compared to the simulation data for that condition in Figure 8(b). For this condition, the simulation results slightly overpredicted the experimental performance at times less than about 300 seconds and under predicted the experimental performance at times greater than about 300 seconds. This over- and underprediction tends to average out. The AA%E and the  $R^2$  values are both better than the experimental error. Figure 8(c) shows the same information for an inlet flow rate of 60 slpm. For this case, the simulation under predicted the experimental performance across the entire time domain. However, the error between the experiment and the prediction is still better than the experimental error as can be seen in (3)–(18). The systematic deviation indicated that the kinetic model included a rate expression that was somewhat too high; however, the comparable duration to breakthrough indicated that the  $\text{CO}_2$  adsorption capacity was quite accurate. Rather than use the CFD model to adjust the imperfect rate expression, it was decided to conduct a parametric analysis on the rates and use the best rate parameters to evaluate the hydrodynamics and mixing.

Another way to compare the model is to calculate and compare the total  $\text{CO}_2$  adsorbed for the simulations and the



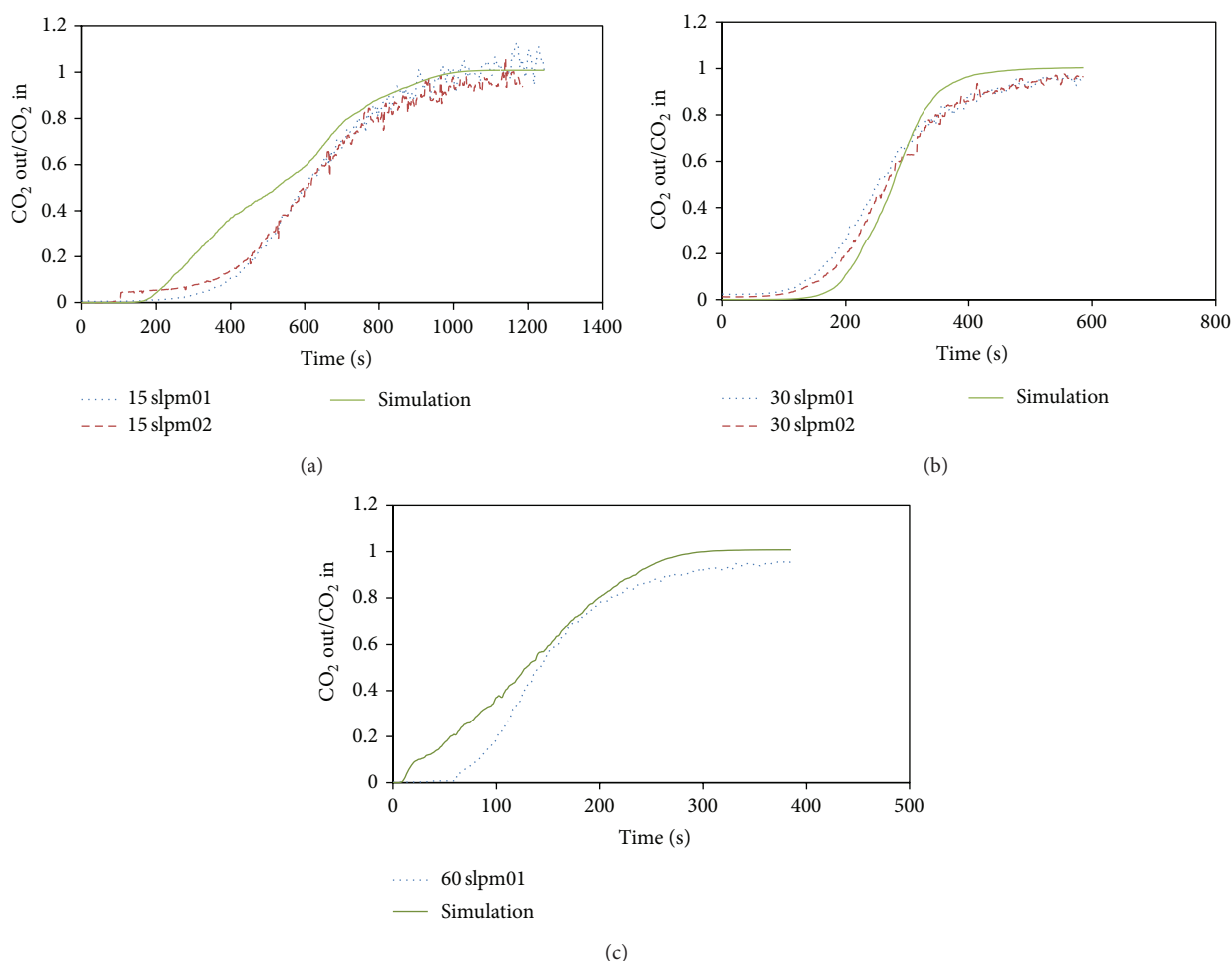


FIGURE 8: Comparison of simulated and experimental breakthrough at different gas flow rates: (a) 15 slpm, (b) 30 slpm, and (c) 60 slpm gas flow.

experiments. This quantity is calculated by subtracting the values in Figure 8 from a value of 1 and then integrating to determine the area under the curves. These areas are shown in Figure 9 as a function of the feed gas flow rate. For the flow rates of 15 and 30 slpm, the simulation results were bounded by the experimental values. The deviation between the experimental value and the simulation value is within the error range as defined by the data spread for the 15 slpm case. Converting these values to a capacity and averaging the experimental values and the simulation values gives an experimental capacity of  $2.61 \pm 0.22/-0.31$  moles/kg of sorbent and a simulation capacity of  $2.61 \pm 0.11/-0.07$  moles/kg of sorbent. These values compare with the theoretical material property of  $2.7 \pm 0.1$  moles/kg of sorbent.

**5.3. Parameter Sensitivity.** In this discussion, three different aspects of the CFD model are explored to better understand the behavior of the model: reaction rate, particle size, and distributor plate design. This will be useful in future studies

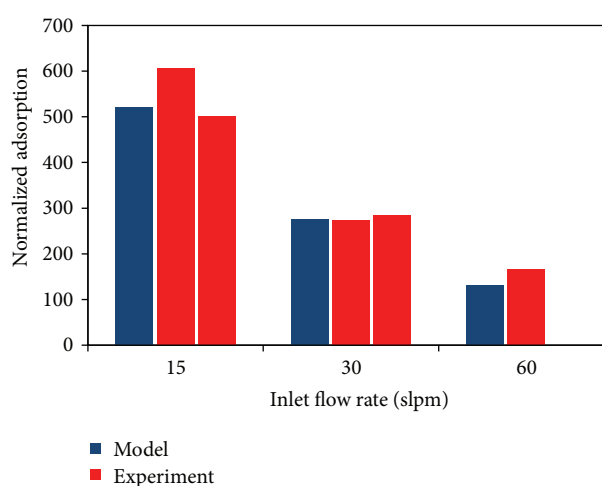


FIGURE 9: Normalized adsorption.

and to provide suggestions on how to improve the agreement between the measured and predicted CO<sub>2</sub> profiles.

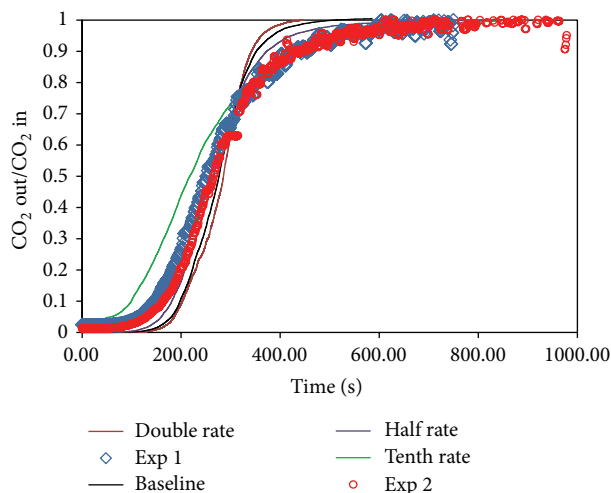


FIGURE 10: Effect of reaction rate on point to point variance between predicted and experimental measurements.

CFD simulations were performed using a scaled value of the kinetic rate preexponential value. The results of these simulations are presented in Figure 10. In this figure, the same information presented in Figure 8(b) is accompanied by simulations where the Arrhenius preexponential factor was modified by first doubling it and halving it. Halving this factor reduced the point to point variance from an absolute average value of 5.3% to 3.7%. Doubling the preexponential factor increased the point to point variance to an absolute average value of 6.1%. Since halving the rate improved the point to point variance, a simulation was run at one tenth the rate to provide a minimum boundary. The point to point average variance for the simulation case with the rate taken as one tenth the ADA fitted rate is 4.95%. The rate is too low as the curve at low conversions was to the right of the experimental data and with this slower rate is to the left of the experimental data as can be seen in Figure 10. Looking at the simulation results and the experimental data in Figure 10, it is estimated that the rate obtained from the ADA performance [22] is between four and six times too fast for the sorbent used in these studies. This difference may partially be attributed to external mass transfer effects.

The effect of particle size has been explored and the results presented in Figure 11 with respect to the baseline. In this figure, the normalized exit  $\text{CO}_2$  in the exit stream is plotted against time as was done in previous plots (Figures 8 and 10). The  $\text{CO}_2$  breakthrough results for the simulated case using  $300\ \mu\text{m}$  particles is compared with the experimental data and the base case simulation results using the same symbol and line pattern as used in Figure 10. The  $300\ \mu\text{m}$  simulation results produce a steeper curve. According to the analysis presented in Figure 10, the rate of removal for the larger particles is faster than that for the smaller base case particles. This is because the reaction rate is independent of the particle size, thus the difference in the bed fluidization state.

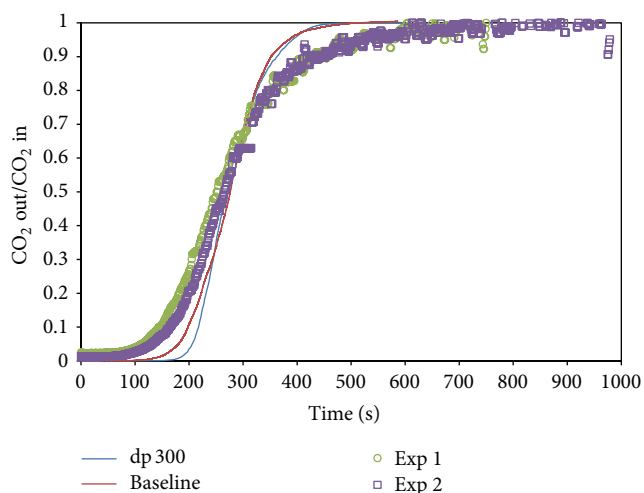


FIGURE 11: Effect of particle size.

Hydrodynamics results are presented in Figures 12 and 13. These figures from left to right present the solids fraction, the gas velocity, and the particle species (with and without the diluents, FCC). The base case with smaller particles (Figure 12) has a bed that is about 20% more expanded than that for the larger particles (Figure 13). This is consistent with the excess gas velocity. The data in Figure 12 was obtained at a level  $U/U_{mf}$  value of about 16 whereas the data in Figure 14 was obtained at a  $U/U_{mf}$  value of 1.5. The base case produced higher and nonuniform gas velocity, while the larger particles exhibited lower and more uniform gas velocity. Also, the distribution of the reacting particles for the larger particles is more uniform within the region of reacting particles. In summary, these results indicate that the hydrodynamics for larger particles lead to a delayed breakthrough of the  $\text{CO}_2$  with a more compressed adsorption zone which exhibits less  $\text{CO}_2$  reactivity in both the leading and trailing edges of that zone.

In the experimental unit, the fluidizing gas is not uniformly injected across the entire cross section. This is the result of the solids withdrawal system when operating the reactor in a continuous manner. To assess the effect this might have on the simulated results, a simulation case was run where the gas was injected into the annular region comparable to the experimental setup. The results from this simulation are shown in Figure 14 along with the corresponding experimental data and the base simulation. The rate of reaction for the modified distributor is greater than that for the base simulation. This again is primarily due to the hydrodynamics in the modified simulation. Compared to the base case, the simulation with the modified distributor plate has more uniform distribution of the reactive species as seen by examining Figures 15 and 12 together. Also, the gas flow is uniformly distributed over the annular region where the reactive solids are located. These combined effects lead to a narrower reaction zone with less bypassing in the leading and trailing regions prior to and following breakthrough.

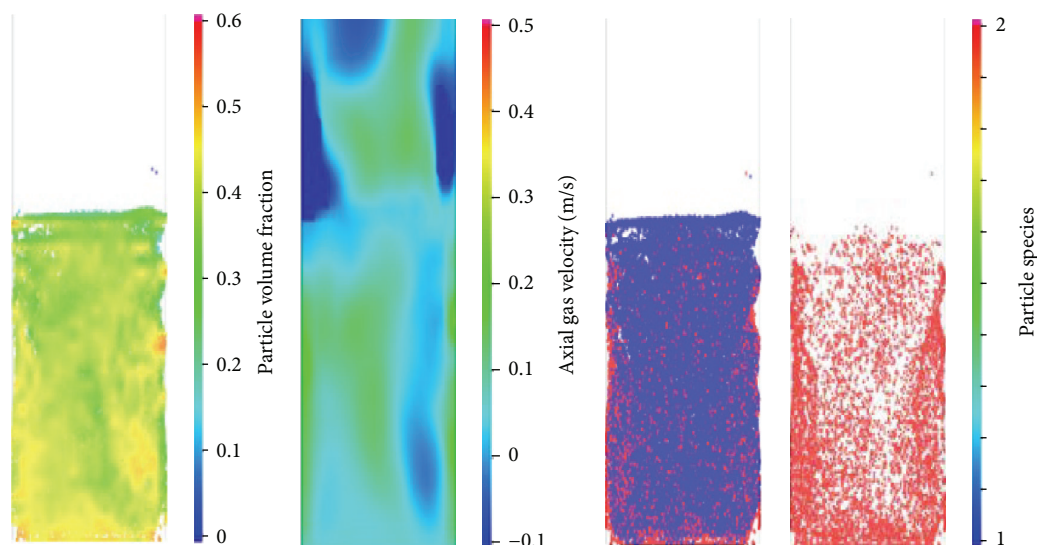


FIGURE 12: Bed hydrodynamic condition for base case simulation with  $d_p = 150 \mu\text{m}$  (solids fraction, gas velocity, particle positions colored by species id 1-amine, 2-FCC).

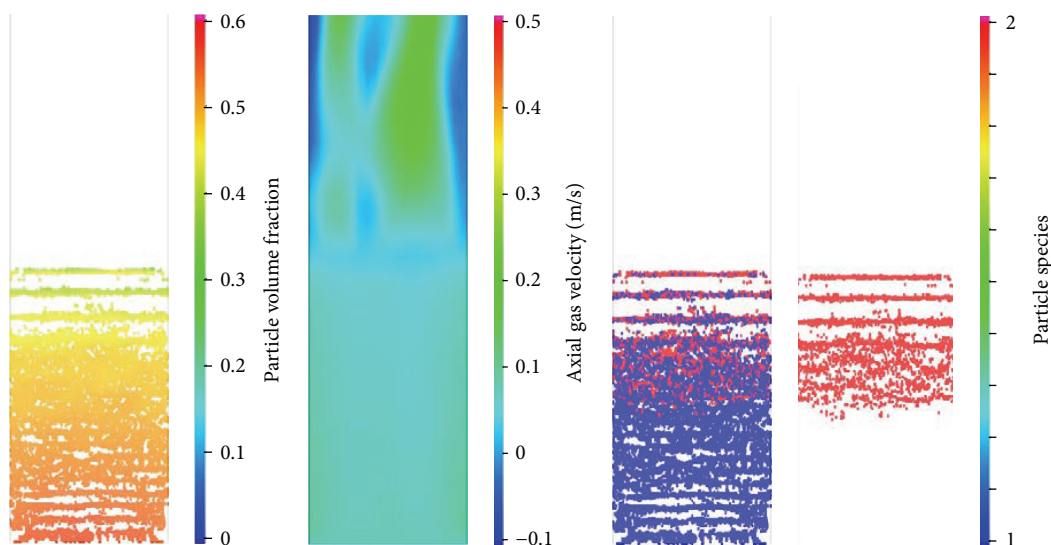


FIGURE 13: Bed hydrodynamic condition for larger particle size,  $d_p = 300 \mu\text{m}$  (solids fraction, gas velocity, particle positions colored by species id 1-amine, 2-FCC).

The measured pressure drop across the fluidized bed was 0.63 kPa compared to the simulated value of 0.80 kPa. This represents only 58 and 70% of the weight of the mixture in the fluid beds. The simulation was able to capture some of the causes for this. In Figure 12 it is apparent that the FCC collected in the center stagnant region while the sorbent was concentrated in the annular regions of the cylindrical bed. This type of segregation and channeling explains why the capacity of the sorbent did not suffer from the stagnation in the center. The sorbent was apparently always available to absorb  $\text{CO}_2$  from the flowing gas. The simulation did not include the heat exchange coils and this may explain why the pressure-drop for the hydrodynamically supported solids was higher than that measured experimentally.

## 6. Conclusions

It has been shown that the Barracuda code by CPFD software can be used to simulate the performance of a fluidized bed reacting system for the adsorption of  $\text{CO}_2$  on a supported polyamine sorbent material. The code accurately predicted the breakthrough time and the sorbent capacity within the experimental error as defined by repeat experiments. The Barracuda model was able to capture the channeling and segregation of the mixture producing a pressure drop that represented 70% of the weight of the bed, while the experiments measured a pressure drop of about 60% of the weight of the bed. However, the segregation did not affect the capacity of the sorbent either experimentally or in the CFD model.

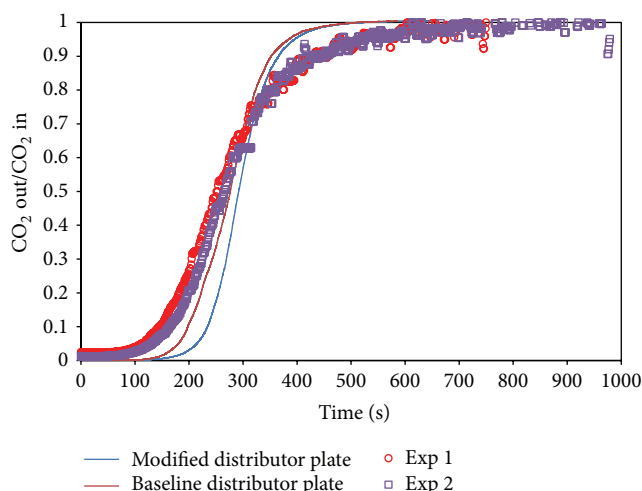


FIGURE 14: Effect of distributor plate design.

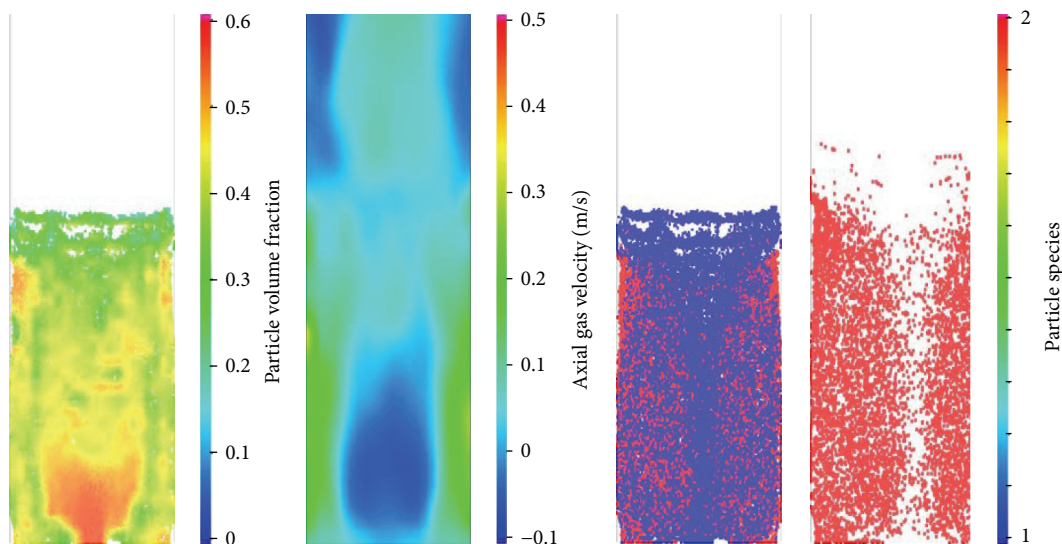


FIGURE 15: Bed hydrodynamic condition for modified distributor plate design (solids fraction, gas velocity, particle positions colored by species id 1-amine, 2-FCC).

indicating that the sorbent remained in the gas flow path. The theoretical capacity of the sorbent material was  $2.7 \pm 0.1$  moles/kg of sorbent. The experiments gave an average result within that experimental error of  $2.61 + 0.22/-0.31$ . The simulation results averaged to the same value as the experimental results, but with tighter deviation as defined by the range for the three conditions with the simulation results being  $2.61 + 0.11/-0.07$  moles/kg of sorbent.

Application of the model to other cases revealed that the predicted bed reactivity (or effective reaction rate) is about four to six times higher than the observed experimental rates. The parameter sensitivity studies suggest a number of paths for further improvement of the model, including the reformulation and subsequent calibration of a particle reaction

model. This work has been started and should be concluded early next year. It was also shown that a nonuniform solids distribution and contacting gas velocity distribution results in a decrease in the size of the adsorption zone while reducing  $\text{CO}_2$  bypassing. In comparing the experimental pressure drop across the reactor to the predicted from the simulations, it is concluded that the model should be expanded to explicitly resolve the internal heat transfer internal surfaces. The interaction of the heat transfer surfaces with the nonuniform fluidization will provide a channeling path for the gas, decreasing the overall bed reactivity. It is anticipated that further improvements to the overall predictive capability will be provided by including local temperature variations which will affect the reaction rate and  $\text{CO}_2$ -absorption capacity.



## Disclaimer

The U.S. Department of Energy, NETL contributions to this report were prepared as an account of work sponsored by an agency of the United States Government. Neither the United States Government nor any agency thereof, nor any of their employees, makes any warranty, express or implied, or assumes any legal liability or responsibility for the accuracy, completeness, or usefulness of any information, apparatus, product, or process disclosed, or represents that its use would not infringe privately owned rights. Reference herein to any specific commercial product, process, or service by trade name, trademark, manufacturer, or otherwise does not necessarily constitute or imply its endorsement, recommendation, or favoring by the United States Government or any agency thereof. The views and opinions of authors expressed herein do not necessarily state or reflect those of the United States Government or any agency thereof.

## Conflict of Interests

The authors declare no competing financial interest.

## Acknowledgments

The authors would like to thank the Carbon Capture and Sequestration funding for the operations of the C2U. In addition, the experimentalists are grateful for the efforts of Rupen Panday who developed and maintained the data acquisition and control systems for that unit, McMahan Gray who provided the sorbent, and Jonathan Tucker who conducted sorbent characterization tests.

## References

- [1] J.-M. Barnola, D. Raynaud, C. Lorius, and N. I. Barkov, "Historical CO<sub>2</sub> record from the Vostok ice core," in *Trends: A Compendium of Data on Global Change*, Carbon Dioxide Information Analysis Center, Oak Ridge National Laboratory, U.S. Department of Energy, Oak Ridge, Tenn, U.S.A., 2003.
- [2] J. Hansen, M. Sato, and R. Ruedy, "Global Temperature Update Through 2013," 2014, <http://www.columbia.edu/~jeh1/mailings/2014/20140121-Temperature2013.pdf>.
- [3] E. Dlugokencky and P. Tans, NOAA/ESRL, <http://www.esrl.noaa.gov/gmd/ccgg/trends/>.
- [4] J. Ciferno, J. Litynski, L. Brickett et al., *DOE/NETL Advanced CO<sub>2</sub> Capture R&D Program: Technology Update*, U.S. Department of Energy, 2011.
- [5] T. F. Wall, "Combustion processes for carbon capture," *Proceedings of the Combustion Institute*, vol. 31, pp. 31–47, 2007.
- [6] A. A. Olajire, "CO<sub>2</sub> capture and separation technologies for end-of-pipe applications—a review," *Energy*, vol. 35, no. 6, pp. 2610–2628, 2010.
- [7] M. B. Toftagaard, J. Brix, P. A. Jensen, P. Glarborg, and A. D. Jensen, "Oxy-fuel combustion of solid fuels," *Progress in Energy and Combustion Science*, vol. 36, no. 5, pp. 581–625, 2010.
- [8] E. J. Anthony, "Solid looping cycles: a new technology for coal conversion," *Industrial and Engineering Chemistry Research*, vol. 47, no. 6, pp. 1747–1754, 2008.
- [9] J. Blamey, E. J. Anthony, J. Wang, and P. S. Fennell, "The calcium looping cycle for large-scale CO<sub>2</sub> capture," *Progress in Energy and Combustion Science*, vol. 36, no. 2, pp. 260–279, 2010.
- [10] N. Rodríguez, M. Alonso, J. C. Abanades et al., "Comparison of experimental results from three dual fluidized bed test facilities capturing CO<sub>2</sub> with CaO," *Energy Procedia*, vol. 4, pp. 393–401, 2011.
- [11] A. Sayari, Y. Belmabkhout, and R. Serna-Guerrero, "Flue gas treatment via CO<sub>2</sub> adsorption," *Chemical Engineering Journal*, vol. 171, no. 3, pp. 760–774, 2011.
- [12] M. M. F. Hasan, R. C. Baliban, J. A. Elia, and C. A. Floudas, "Modeling, simulation, and optimization of postcombustion CO<sub>2</sub> capture for variable feed concentration and flow rate. 2. Pressure swing adsorption and vacuum swing adsorption processes," *Industrial and Engineering Chemistry Research*, vol. 51, no. 48, pp. 15665–15682, 2012.
- [13] A. L. Chaffee, G. P. Knowles, Z. Liang, J. Zhang, P. Xiao, and P. A. Webley, "CO<sub>2</sub> capture by adsorption: Materials and process development," *International Journal of Greenhouse Gas Control*, vol. 1, no. 1, pp. 11–18, 2007.
- [14] J. Schell, N. Casas, D. Marx, and M. Mazzotti, "Precombustion CO<sub>2</sub> capture by pressure swing adsorption (PSA): comparison of laboratory PSA experiments and simulations," *Industrial and Engineering Chemistry Research*, vol. 52, no. 24, pp. 8311–8322, 2013.
- [15] L. Wang, Y. Yang, W. Shen et al., "CO<sub>2</sub> capture from flue gas in an existing coal-fired power plant by two successive pilot-scale VPSA units," *Industrial & Engineering Chemistry Research*, vol. 52, no. 23, pp. 7947–7955, 2013.
- [16] G. D. Pirngruber and D. Leinekugel-Le-Cocq, "Design of a pressure swing adsorption process for postcombustion CO<sub>2</sub> capture," *Industrial and Engineering Chemistry Research*, vol. 52, no. 17, pp. 5985–5996, 2013.
- [17] R. V. Siriwardane, C. Robinson, M. Shen, and T. Simonyi, "Novel regenerable sodium-based sorbents for CO<sub>2</sub> capture at warm gas temperatures," *Energy & Fuels*, vol. 21, no. 4, pp. 2088–2097, 2007.
- [18] D. J. Fauth, M. L. Gray, H. W. Pennline, H. M. Krutka, S. Sjöstrom, and A. M. Ault, "Investigation of porous silica supported mixed-amine sorbents for post-combustion CO<sub>2</sub> capture," *Energy and Fuels*, vol. 26, no. 4, pp. 2483–2496, 2012.
- [19] M. L. Gray, K. J. Champagne, D. Fauth, J. P. Baltrus, and H. Pennline, "Performance of immobilized tertiary amine solid sorbents for the capture of carbon dioxide," *International Journal of Greenhouse Gas Control*, vol. 2, no. 1, pp. 3–8, 2008.
- [20] M. L. Gray, J. S. Hoffman, D. C. Hreha et al., "Parametric study of solid amine sorbents for the capture of carbon dioxide," *Energy and Fuels*, vol. 23, pp. 4840–4844, 2012.
- [21] A. Lee, D. Mebane, D. J. Fauth, and D. C. Miller, "A model for the adsorption kinetics of CO<sub>2</sub> on amine-impregnated mesoporous sorbents in the presence of water," in *Proceedings of the 28th Annual International Pittsburgh Coal Conference (PCC '11)*, pp. 355–365, September 2011.
- [22] S. Sjöstrom, H. Krutka, T. Starns, and T. Campbell, "Pilot test results of post-combustion CO<sub>2</sub> capture using solid sorbents," *Energy Procedia*, vol. 4, pp. 1584–1592, 2011.
- [23] S. Sjöstrom and H. Krutka, "Evaluation of solid sorbents as a retrofit technology for CO<sub>2</sub> capture," *Fuel*, vol. 89, no. 6, pp. 1298–1306, 2010.
- [24] E. R. Monazam, J. Spenik, and L. J. Shadle, "Fluid bed adsorption of carbon dioxide on immobilized polyethylenimine (PEI):



- kinetic analysis and breakthrough behavior," *Chemical Engineering Journal*, vol. 223, pp. 795–805, 2013.
- [25] A. Samanta, A. Zhao, G. K. H. Shimizu, P. Sarkar, and R. Gupta, "Post-combustion CO<sub>2</sub> capture using solid sorbents: a review," *Industrial & Engineering Chemistry Research*, vol. 51, no. 4, pp. 1438–1463, 2012.
- [26] S. Choi, J. H. Drese, and C. W. Jones, "Adsorbent materials for carbon dioxide capture from large anthropogenic point sources," *ChemSusChem*, vol. 2, no. 9, pp. 796–854, 2009.
- [27] J. S. Hoffman, G. A. Richards, H. W. Pennline, D. Fischer, and G. Keller, "Factors in reactor design for carbon capture with solid regenerable sorbents," in *Proceedings of the 33rd International Technical Conference on Coal Utilization and Fuel Systems*, Clearwater, Fla, USA, June 2008.
- [28] E. R. Monazam, J. Spenik, and L. J. Shadle, "CO<sub>2</sub> desorption kinetics for immobilized polyethylenimine (PEI)," *Energy and Fuels*, vol. 28, no. 1, pp. 650–656, 2014.
- [29] E. R. Monazam, L. J. Shadle, D. C. Miller et al., "Equilibrium and kinetics analysis of carbon dioxide capture using immobilized amine on a mesoporous silica," *AIChE Journal*, vol. 59, no. 3, pp. 923–935, 2013.
- [30] R. Garg, E. D. Huckaby, and M. Shahnam, "CFD simulation of CO<sub>2</sub> capture by solid sorbent," in *Proceedings of the 7th International Conference on Multiphase Flow*, vol. 30, Tampa, Fla, USA, May–June 2010.
- [31] K. K. Saha and E. D. Huckaby, "Eulerian-Eulerian simulations of dual fluidized bed reactor for CO<sub>2</sub> capture," in *Proceedings of the AIChE Annual Meeting*, October 2011.
- [32] R. W. Breault and E. D. Huckaby, "Parametric behavior of a CO<sub>2</sub> capture process: CFD simulation of solid-sorbent CO<sub>2</sub> absorption in a riser reactor," *Applied Energy*, vol. 112, pp. 224–234, 2013.
- [33] E. M. Ryan, D. DeCroix, R. Breault et al., "Multi-phase CFD modeling of solid sorbent carbon capture system," *Powder Technology*, vol. 242, pp. 117–134, 2013.
- [34] E. Abbasi and H. Arastoopour, "CFD simulation of CO<sub>2</sub> sorption in a circulating fluidized bed using deactivation kinetic model," in *Proceedings of the 10th International Conference on Circulating Fluidized Beds and Fluidization Technology*, May 2011.
- [35] LLC CS, *Barracuda—Computational Particle Fluid Dynamics*, 2009, <http://www.cpdf-software.com/>.
- [36] M. J. Andrews and P. J. O'Rourke, "The multiphase particle-in-cell (MP-PIC) method for dense particulate flows," *International Journal of Multiphase Flow*, vol. 22, no. 2, pp. 379–402, 1996.
- [37] D. M. Snider, "An incompressible three-dimensional multiphase particle-in-cell model for dense particle flows," *Journal of Computational Physics*, vol. 170, no. 2, pp. 523–549, 2001.
- [38] P. J. O'Rourke and D. M. Snider, "An improved collision damping time for MP-PIC calculations of dense particle flows with applications to polydisperse sedimenting beds and colliding particle jets," *Chemical Engineering Science*, vol. 65, no. 22, pp. 6014–6028, 2010.
- [39] D. M. Snider, S. M. Clark, and P. J. O'Rourke, "Eulerian-Lagrangian method for three-dimensional thermal reacting flow with application to coal gasifiers," *Chemical Engineering Science*, vol. 66, no. 6, pp. 1285–1295, 2011.
- [40] D. Snider and S. Banerjee, "Heterogeneous gas chemistry in the CPFD Eulerian-Lagrangian numerical scheme (ozone decomposition)," *Powder Technology*, vol. 199, no. 1, pp. 100–106, 2010.
- [41] T. B. Anderson and R. Jackson, "Fluid mechanical description of fluidized beds. Equations of motion," *Industrial & Engineering Chemistry Fundamentals*, vol. 6, no. 4, pp. 527–539, 1967.
- [42] R. Jackson, *The Dynamics of Fluidized Particles*, Cambridge University Press, Cambridge, UK, 2000.
- [43] J. Smagorinsky, "General circulation experiments with the primitive equations," *Monthly Weather Review*, vol. 91, no. 3, pp. 99–164, 1963.

